

# The hemispheric contrast in cloud microphysical properties constrains aerosol forcing

Isabel L. McCoy<sup>a,1,2</sup>, Daniel T. McCoy<sup>b,1,3</sup>, Robert Wood<sup>a</sup>, Leighton Regayre<sup>b</sup>, Duncan Watson-Parris<sup>c</sup>, Daniel P. Grosvenor<sup>b,d</sup>, Jane P. Mulcahy<sup>e</sup>, Yongxiang Hu<sup>f</sup>, Frida A.-M. Bender<sup>g,h</sup>, Paul R. Field<sup>b,e</sup>, Kenneth S. Carslaw<sup>b</sup>, and Hamish Gordon<sup>b,i</sup>

<sup>a</sup>Atmospheric Sciences Department, University of Washington, Seattle, WA 98105; <sup>b</sup>Institute for Climate and Atmospheric Science, School of Earth and Environment, University of Leeds, LS2 9JT Leeds, United Kingdom; <sup>c</sup>Department of Physics, University of Oxford, OX1 3PU Oxford, United Kingdom; <sup>d</sup>National Center for Atmospheric Science, University of Leeds, LS2 9JT Leeds, United Kingdom; <sup>e</sup>Met Office, Exeter EX1 3PB, United Kingdom; <sup>f</sup>Atmospheric Composition Branch, NASA Langley Research Center, Hampton, VA 23681; <sup>g</sup>Department of Meteorology, Stockholm University, SE-106 91 Stockholm, Sweden; <sup>h</sup>Bolin Centre for Climate Research, Stockholm University, SE-106 91 Stockholm, Sweden; and <sup>i</sup>College of Engineering, Carnegie-Mellon University, Pittsburgh, PA 15213

Edited by John H. Seinfeld, California Institute of Technology, Pasadena, CA, and approved June 9, 2020 (received for review December 21, 2019)

The change in planetary albedo due to aerosol–cloud interactions during the industrial era is the leading source of uncertainty in inferring Earth’s climate sensitivity to increased greenhouse gases from the historical record. The variable that controls aerosol–cloud interactions in warm clouds is droplet number concentration. Global climate models demonstrate that the present-day hemispheric contrast in cloud droplet number concentration between the pristine Southern Hemisphere and the polluted Northern Hemisphere oceans can be used as a proxy for anthropogenically driven change in cloud droplet number concentration. Remotely sensed estimates constrain this change in droplet number concentration to be between  $8\text{ cm}^{-3}$  and  $24\text{ cm}^{-3}$ . By extension, the radiative forcing since 1850 from aerosol–cloud interactions is constrained to be  $-1.2\text{ W}\cdot\text{m}^{-2}$  to  $-0.6\text{ W}\cdot\text{m}^{-2}$ . The robustness of this constraint depends upon the assumption that pristine Southern Ocean droplet number concentration is a suitable proxy for preindustrial concentrations. Droplet number concentrations calculated from satellite data over the Southern Ocean are high in austral summer. Near Antarctica, they reach values typical of Northern Hemisphere polluted outflows. These concentrations are found to agree with several in situ datasets. In contrast, climate models show systematic underpredictions of cloud droplet number concentration across the Southern Ocean. Near Antarctica, where precipitation sinks of aerosol are small, the underestimation by climate models is particularly large. This motivates the need for detailed process studies of aerosol production and aerosol–cloud interactions in pristine environments. The hemispheric difference in satellite estimated cloud droplet number concentration implies preindustrial aerosol concentrations were higher than estimated by most models.

cloud droplet number concentration | radiative forcing | aerosol–cloud interactions | Southern Ocean | remote sensing

The change in reflected shortwave radiation between the preindustrial (PI) and the present day (PD) due to anthropogenic emissions of aerosols, known as aerosol radiative forcing, is the leading cause of uncertainty in inferring climate sensitivity from the observational record (1, 2). A recent survey identified the dominant contributor to the uncertainty in global mean aerosol radiative forcing as aerosol–cloud interactions (aci) in liquid clouds (3). Aerosols change the radiation reflected back to space by liquid clouds in two ways: 1) by modulating the number concentration of cloud droplets ( $N_d$ ), which changes cloud reflectivity even without any changes to cloud macrostructure (4); 2) by changing  $N_d$ , cloud microphysical processes are altered that have various impacts on cloud macrophysical properties [e.g., cloud cover or liquid water content (5)]. These effects are referred to as radiative forcing due to aci ( $RF_{aci}$ ) and cloud adjustments to aerosol, respectively (6). The combined forcing from aerosol–cloud adjustments and  $RF_{aci}$  is referred to as the effective  $RF_{aci}$  ( $ERF_{aci}$ ). The net aerosol forcing is the sum of  $ERF_{aci}$  and a similar quantity

for aerosol direct interactions,  $ERF_{dir}$ . Here, we focus on providing an observational constraint for the change in  $N_d$  and  $RF_{aci}$ . The forcing due to aerosol–cloud adjustments is uncertain in both sign and magnitude (7–13), but is expected to scale with changes in  $N_d$  (3). Narrowing the possible range of changes in  $N_d$  and resulting  $RF_{aci}$  will narrow uncertainty in  $ERF_{aci}$  and, by extension, improve our inference of climate sensitivity (1, 3).

$RF_{aci}$  is nonlinearly dependent on the change in  $N_d$  over the industrial period (14). Natural aerosols, or aerosols in the PI state, are the largest cause of uncertainty in aerosol forcing over the industrial period (14, 15). The PD  $N_d$  is observable, but we must infer PI  $N_d$  using other means. Here, we use the pristine Southern Hemisphere (SH) (16) as a proxy for the PI and examine the contrast between the SH and the polluted Northern Hemisphere (NH) to estimate the anthropogenic perturbation to  $N_d$ .

## Significance

Enhancement of aerosol that can nucleate cloud droplets increases the droplet number concentration and albedo of clouds. This increases the amount of sunlight reflected to space. Uncertainty in how aerosol–cloud interactions over the industrial period have increased planetary albedo by this mechanism leads to significant uncertainty in climate projections. Our work presents a method for observationally constraining the change in albedo due to anthropogenic aerosol emissions: a hemispheric difference in remotely sensed cloud droplet number between the pristine Southern Ocean (a preindustrial proxy) and the polluted Northern Hemisphere. Application of this constraint to climate models reduces the range of estimated albedo change since industrialization and suggests current models underpredict cloud droplet number concentration in the preindustrial era.

Author contributions: I.L.M., D.T.M., and R.W. designed research; I.L.M., D.T.M., and R.W. performed research; L.R., D.W.-P., D.P.G., J.P.M., P.R.F., and K.S.C. contributed new reagents/analytic tools; I.L.M., D.T.M., R.W., L.R., D.W.-P., Y.H., F.A.-M.B., and H.G. analyzed data; I.L.M., D.T.M., R.W., and L.R. wrote the paper; and I.L.M., D.T.M., R.W., L.R., D.W.-P., D.P.G., J.P.M., Y.H., F.A.-M.B., P.R.F., K.S.C., and H.G. contributed ideas.

The authors declare no competing interest.

This article is a PNAS Direct Submission.

This open access article is distributed under [Creative Commons Attribution License 4.0 \(CC BY\)](https://creativecommons.org/licenses/by/4.0/).

<sup>1</sup>I.L.M. and D.T.M. contributed equally to this work.

<sup>2</sup>To whom correspondence may be addressed. Email: imccoy@uw.edu.

<sup>3</sup>Present address: Department of Atmospheric Science, University of Wyoming, Laramie, WY 82071.

This article contains supporting information online at <https://www.pnas.org/lookup/suppl/doi:10.1073/pnas.1922502117/-DCSupplemental>.

First published July 27, 2020.

Previous studies have discussed the hemispheric contrast in cloud properties created by anthropogenic aerosol emissions in the NH. The effective radius of droplets ( $r_e$ ) is smaller in the NH than in the SH (17, 18). Feng and Ramanathan (18) found that a chemical transport model driven by reanalysis meteorology was able to produce a difference in  $N_d$  between the NH and SH consistent with hemispheric contrasts in satellite retrievals of  $r_e$  and cloud optical depth ( $\tau$ ). Boucher and Lohmann (19) used the hemispheric difference in  $r_e$  to evaluate the robustness of the  $RF_{aci}$  simulated in instances of the LMD (Laboratoire de Météorologie Dynamique) and ECHAM (European Center for Medium-range Weather Forecasting, Hamburg version) global climate models (GCMs) when a prescribed relationship between sulfate mass and  $N_d$  was implemented. As in these pioneering works, we use hemispheric differences in cloud microphysics to evaluate modeled aci. Our approach differs from previous work in the following ways. First,  $r_e$ , while readily retrieved by remote sensing, is a function of both the number concentration of cloud condensation nuclei (CCN) and the liquid water content of clouds. The differences in cloud liquid water content between hemispheres (18, 20) will weaken any  $r_e$ -based constraint on hemispheric CCN difference.  $N_d$  is calculated from remote sensing retrievals of both  $r_e$  and  $\tau$ , which helps to account for cloud liquid water contributions as outlined in Grosvenor et al. (21). We use this calculated  $N_d$  to constrain  $RF_{aci}$  because it is the key variable linking cloud microphysical and aerosol properties (22). Second, we analyze output from a large collection of GCMs designed to quantify aerosol forcing alongside a million-member ensemble from a single model that samples uncertainty in 26 aerosol processes (23). This enables us to robustly quantify and then constrain the uncertainty in the change in  $N_d$  and  $RF_{aci}$ .

The  $N_d$  derived from satellite retrievals has been shown to be reasonably unbiased in comparison with aircraft measurements (21, 24–28) and to agree well in both the remote Southern Ocean (SO) (29) and the NH (28). Biases between in situ and  $N_d$  calculated based on Moderate Resolution Spectroradiometer (MODIS) data are on the order of  $1\text{ cm}^{-3}$  to  $20\text{ cm}^{-3}$ , depending on geographic region and boundary layer stratification, and systematic bias does not scale strongly with  $N_d$  (27–29). The hemispheric contrast in  $N_d$  is a difference, so this should moderate the effects of any systematic biases in  $N_d$ . Our understanding of the relationship between hemispheric contrast in  $N_d$  and anthropogenic perturbations to  $N_d$  is facilitated by insight into the uncertainty in the PI atmosphere provided by GCMs. We combine analysis of structural model uncertainty from CMIP5 models participating in the AeroCom phase II project (30) and several simulations made during the development of the atmosphere-only climate model configuration, HadGEM3-GA7.1 (Hadley Center Global Environmental Model) (31) with analysis of parametric uncertainty within a perturbed parameter ensemble (PPE) in HadGEM3-GA4-UKCA (United Kingdom Chemistry and Aerosols). The PPE is based on 235 individual simulations in which combinations of 26 aerosol processes and emissions were perturbed (23). The output from these 235 simulations was used to train Gaussian process emulators to enable a million model variants to be generated, facilitating more robust statistical analysis (32). We show that uniting this growing confidence in satellite-derived  $N_d$  with state-of-the-art modeling experiments directed at evaluating aci in warm clouds allows us to bound anthropogenic perturbations to  $N_d$  and  $RF_{aci}$  over the industrial period.

## Results

**Definition and Application of a Hemispheric Contrast.** Comparing satellite-derived, maritime  $N_d$  from MODIS with AeroCom phase II and HadGEM3-GA7.1 development simulations reveals major discrepancies between GCMs and MODIS  $N_d$  in the PD. GCMs consistently overestimate tropical and NH midlatitude  $N_d$  (Fig. 1A and B). They consistently underestimate summertime  $N_d$  in

the SH midlatitude (30°S to 60°S) (Fig. 14). GCMs also underestimate summertime marine  $N_d$  poleward of 60° in both hemispheres, especially in the SH, where MODIS  $N_d$  increases significantly toward Antarctica (Figs. 14 and 24). Intriguingly, the mean MODIS summertime  $N_d$  near Antarctica is close to values found in continental outflows from heavily industrialized regions (28). The remote SO is among the most pristine regions in the world (16), with emissions from ocean biology controlling aerosol and  $N_d$  seasonality (33, 34). The NH midlatitude has both polluted and pristine aerosol influences. The magnitude of the summertime Arctic MODIS  $N_d$  increase is smaller than the summertime Antarctic increase, possibly due to the closer proximity to large continental and anthropogenic sources of aerosol in the NH [and the nonlinear relationship between CCN and  $N_d$  (14)]. While more complex to disentangle, the natural sources of NH aerosol have a significant seasonal cycle driven by ocean biology (35–37). These high summertime midlatitude and high-latitude satellite-derived  $N_d$  values in the SH and high-latitude satellite-derived  $N_d$  values in the NH are not captured by GCMs but, as discussed below, are supported by in situ observations of CCN and  $N_d$ . PPE model members show similar discrepancies compared with MODIS, although NH values are less overestimated, on average (SI Appendix, Fig. S2).

As there are no observations of PI  $N_d$ , the accuracy of modeled PI  $N_d$  cannot be evaluated directly. However, we are able to draw three qualitative conclusions regarding the PI and PD  $N_d$  from the models. First, in the GCMs, the majority of the PD–PI change is in the NH. This is consistent with the zones of maximum anthropogenic emissions and direct aerosol forcing (18, 38). Second, sources of CCN over the SO are largely marine with very small contributions from continents, and levels that are mostly unchanged from the PI to the PD (16). Third, our analysis of the AeroCom phase II and HadGEM3-GA7.1 development simulations show the PI  $N_d$  is fairly similar in the NH and SH, with a difference in the 30° to 60°-latitude bands over oceans for these simulations of  $16 \pm 7\text{ cm}^{-3}$  at 95% confidence. In contrast, simulated PD  $N_d$  difference between these bands is  $43 \pm 8\text{ cm}^{-3}$  at 95% confidence. The larger PI  $N_d$  in the NH compared to the SH is primarily due to biomass burning emissions in the NH (39). However, the relative hemispheric symmetry in PI  $N_d$  is consistent with modeling studies of aerosol sources over oceans in the PI, where marine sources contribute a large fraction of marine CCN in both hemispheres (40, 41).

Based on our ability to estimate  $N_d$  in the PD from remote sensing retrievals and the aforementioned inferences from GCMs, we can use the hemispheric PD  $N_d$  difference between the polluted NH and the pristine SH oceans to gain insight into the change in global mean area-weighted  $N_d$  between PD and PI over land and ocean ( $\Delta N_{d(PD-PI)}$ ). We find that there is a positive correlation between  $\Delta N_{d(PD-PI)}$  and the differences in marine  $N_d$  between 30°N to 60°N and 30°S to 60°S ( $\Delta N_{d(NH-SH)}$ ) within the various GCMs examined in this study and the members of the PPE (Fig. 1C). Examination of the million-member sample shows that  $\Delta N_{d(NH-SH)}$  is approximately linearly correlated with  $\Delta N_{d(PD-PI)}$  ( $R^2 = 0.3$ ). The AeroCom phase II models fall within the 95% prediction interval of the best fit to the PPE sample members, except for ECHAM6. This may be due to ECHAM6's imposed minimum  $N_d$  of  $40\text{ cm}^{-3}$ , which is near the mean PI  $N_d$  in the GCMs surveyed here (Fig. 1A and B). MODIS estimates  $\Delta N_{d(NH-SH)}$  to be between  $32\text{ cm}^{-3}$  and  $37\text{ cm}^{-3}$  with 95% confidence. To agree with the satellite estimated range and the linear fit to the PPE,  $\Delta N_{d(PD-PI)}$  is predicted to be  $8\text{ cm}^{-3}$  to  $24\text{ cm}^{-3}$  at 95% confidence (Fig. 1C).

The  $\Delta N_{d(PD-PI)}$  predicted by the HadGEM3-GA7.1 development models is on the upper end of what is predicted by the PPE. This is consistent with the stronger  $ERF_{aci}$  in GA7 model versions ( $-2.75\text{ W}\cdot\text{m}^{-2}$  in GA7.0,  $-1.45\text{ W}\cdot\text{m}^{-2}$  in GA7.1) compared to the weaker aerosol forcing in the GA4.0 model version

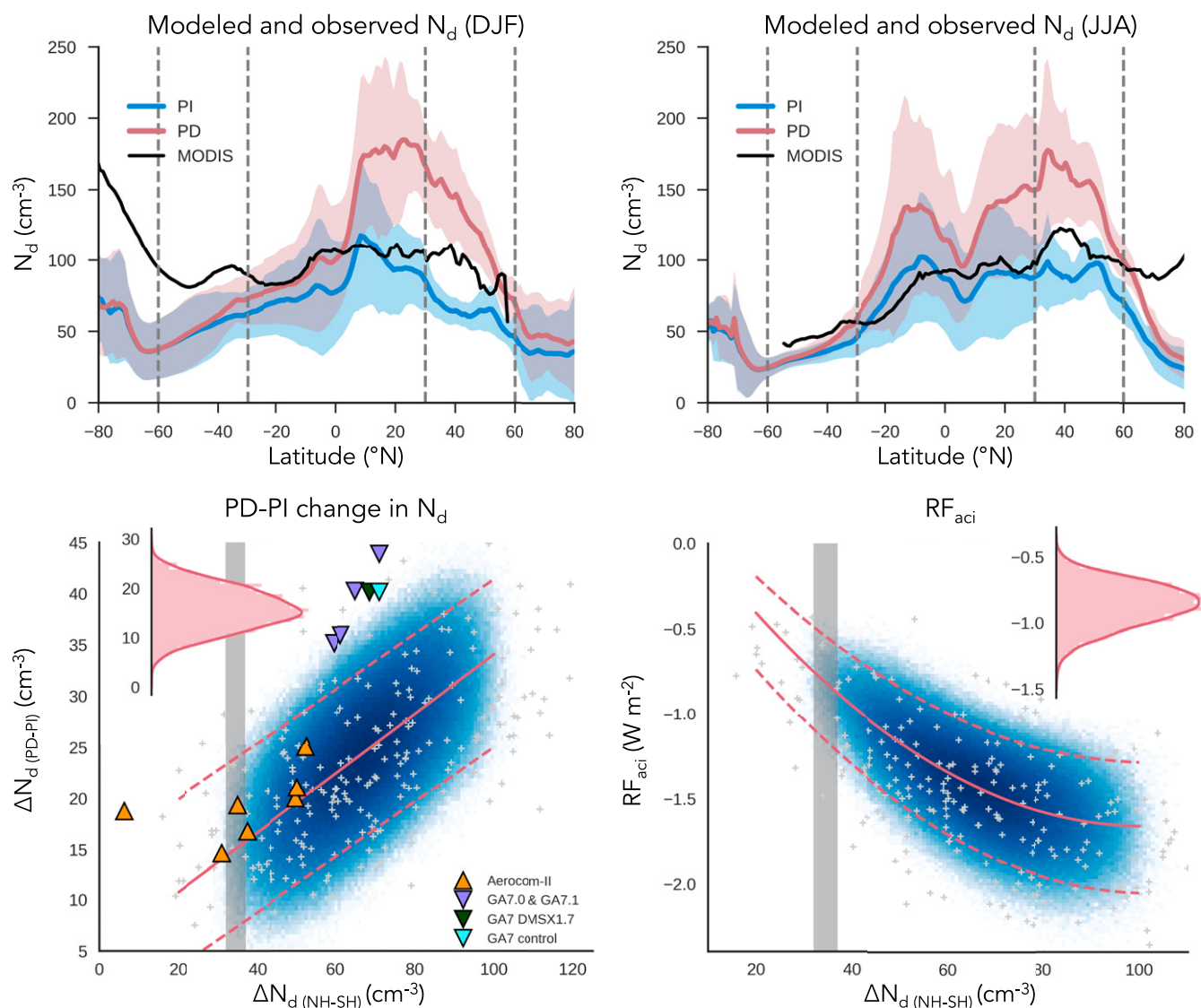


**Fig. 1.** Constraints on aci from satellite estimated hemispheric contrast in  $N_d$  over oceans ( $\Delta N_{d(NH-SH)}$ ). (A and B) Oceanic PI (blue) and PD (red)  $N_d$  modeled by Aerocom-II models and HadGEM3-GA7.1 development models. Thick lines show the multimodel mean, and corresponding shading shows the SD across models. (A and B) Data from (A) December through February (DJF) and (B) June through August (JJA). In SO winter, the Aerocom-II National Center for Atmospheric Research models are missing data due to lack of low, liquid cloud, leading to discontinuity in the multimodel mean at 70°S. Zonal means from each model are shown in *SI Appendix, Fig. S1*.  $\Delta N_{d(NH-SH)}$  is calculated as the difference in annual, area-weighted mean  $N_d$  over the ocean between 30°N to 60°N and 30°S to 60°S (averaging boundaries shown as vertical dashed lines). (C) Change in oceanic  $N_d$  between the PI and PD ( $\Delta N_{d(PD-PI)}$ ) as a function of  $\Delta N_{d(NH-SH)}$  in PPE members (gray crosses for individual model members, blue shading for  $N_d$  values sampled from a statistical emulator), in Aerocom-II (orange triangles), and HadGEM3-GA7.1 development models (purple, blue, and dark green triangles). HadGEM3-GA7.0 with enhanced DMS is shown in dark green and the control HadGEM3-GA7.0 in blue. The linear fit to the PPE data and 95% prediction bands on the fit are shown as red solid and dashed lines. The 95% confidence on the interannual range of  $\Delta N_{d(NH-SH)}$  estimated by MODIS is shown in gray. (D) As in C but showing the relation between  $RF_{aci}$  and the hemispheric contrast calculated from the PPE sample members along with a second-order polynomial fit between  $\Delta N_{d(NH-SH)}$  and  $RF_{aci}$ . (Insets) The PDF of the emulated PPE member values within the observationally constrained range of  $\Delta N_{d(NH-SH)}$  (C) for  $\Delta N_{d(PD-PI)}$  and (D) for  $RF_{aci}$ .

used in the PPE ( $-1.51 \text{ W m}^{-2}$  on average with a 95% credible range of  $-2.04 \text{ W m}^{-2}$  to  $-0.96 \text{ W m}^{-2}$ ) (23, 42). The spread of  $\Delta N_{d(PD-PI)}$  between the PPE, Aerocom, and HadGEM3-GA7 models demonstrates the importance of examining multiple GCMs to consider structural differences. Because few of the GCMs (three of the eight Aerocom models and none of the HadGEM3-GA7 models) are consistent with MODIS  $N_d$ , we also demonstrate the usefulness of sampling uncertainty within a single model by using the PPE. Using the million-member sample helps us to avoid the equifinality issues raised by examining a single model variant (43, 44) and produces a small subset of model variants within the

observational range. Further investigation of the aerosol parameters important in this subset of member variants may help us to understand the processes that are key to producing values of  $N_d$  that are consistent with satellite data.

We have constrained changes in  $\Delta N_{d(PD-PI)}$  using satellite estimated  $\Delta N_{d(NH-SH)}$ . A similar constraint can be applied to  $RF_{aci}$ . The Aerocom phase II and HadGEM3-GA7.1 development models include aerosol–cloud adjustments, so, for this analysis, we rely on our million-member sample from the PPE which has no aerosol–cloud adjustments. We find that the  $RF_{aci}$  is negatively correlated with  $\Delta N_{d(NH-SH)}$  (Fig. 1D). We fit the relationship



between  $RF_{aci}$  and  $\Delta N_{d(NH-SH)}$  in the million-member sample using a second-order polynomial. For large values of  $\Delta N_{d(NH-SH)}$ , the spread in  $RF_{aci}$  from the PPE is very broad. However, when  $N_d$  is more symmetric between hemispheres, the range of  $RF_{aci}$  produced by different members of the PPE narrows. The prediction interval of the fit combined with the satellite estimated  $\Delta N_{d(NH-SH)}$  constrains  $RF_{aci}$  to be between  $-1.2 \text{ W}\cdot\text{m}^{-2}$  and  $-0.6 \text{ W}\cdot\text{m}^{-2}$  at 95% confidence.

One caveat to our constraint on  $RF_{aci}$  and  $\Delta N_{d(PD-PI)}$  is that our methodology may suffer from the same limitations that all single-observation constraints suffer from, which is producing an overly tight constraint (45). However, combining this methodology with other observational constraints may avoid these single observation issues [e.g., as in the multiobservation constraint on  $ERF_{aci}$  in Johnson et al. (45) and Regayre et al. (46)] as well as help to constrain uncertainty associated with other processes in the models not captured by  $\Delta N_{d(NH-SH)}$  (e.g., the aerosol optical depth constraint on  $RF_{aci}$  presented in ref. 32). We have chosen to only use satellite data over oceans in calculating  $\Delta N_{d(NH-SH)}$  because it is more extensively evaluated against aircraft measurements (21). This broadens the constraint on global mean PI to PD changes in cloud properties ( $\Delta N_{d(PD-PI)}$ ) and  $RF_{aci}$  in Fig. 1 C and D, *Insets*) by ignoring information from satellite data over land. However, we choose to use more robust satellite data at the cost of a broader, but more reliable, constraint on global mean changes.

**Evaluating SO  $N_d$ .** The hemispheric constraint depends on the accuracy of the satellite-derived values of PD  $N_d$ . As noted in the Introduction, MODIS  $N_d$  has been extensively validated against aircraft measurements in the NH and parts of the SH (21, 28, 29). Because aircraft observations of  $N_d$  are not as plentiful in the more remote regions of the SO, we use other datasets to provide additional assessment of the quality and the believability of the surprising SO MODIS  $N_d$  pattern (Fig. 2).

The latitudinal and seasonal patterns of MODIS  $N_d$  are supported by the multiyear records of CCN from Antarctic ground sites at King Sejong Station (62°S) (47) and McMurdo Station

(77°S) (48) (Fig. 2 and *SI Appendix*, Fig. S3A). Comparison of MODIS  $N_d$  within 4° of each station to the CCN station data shows matching summertime peaks and an increase with poleward latitude between King Sejong and McMurdo (*SI Appendix*, Fig. S3A). Summertime CCN measured at King Sejong was classified as largely biogenic (49, 50). This is consistent with measurements taken during cruises in the SO that observed increases in CCN, biogenic CCN precursor gases [i.e., phytoplankton emissions of dimethyl sulfide (DMS) which can be oxidized in the atmosphere to form either sulfate, an efficient CCN (19, 33, 51–54), or precursors for particle nucleation] (55), and concentrations of small particles that grow into CCN [i.e., nucleation-mode aerosols, often newly formed from biogenic precursor gases (56, 57)] (58) near Antarctica. The RITS (Radiatively Important Trace Species) campaign (59, 60) also observed a summertime increase in total aerosol concentration (including nucleation and CCN size aerosols) between its winter 1993 and summer 1994 cruises along the coast of Antarctica (*SI Appendix*, Fig. S3 map and *SI Appendix*, Fig. S3B).

We suspect that the summertime peak in  $N_d$  near Antarctica is linked to increases in biological activity as sea ice retreats in these regions. The seasonal sea ice zone's high productivity and frequent, large phytoplankton blooms (61–63) lead to enhanced emissions of biogenic CCN precursor gases. Recent observations found increased concentrations of trace gases associated with DMS oxidation in the seasonal sea ice zone (55), nucleation-mode particles at ice edge (64), and nucleation-mode particles in biologically active basins near Antarctica (49, 50). The 2016 ORCAS ( $\text{O}_2/\text{N}_2$  Ratio and  $\text{CO}_2$  Airborne Southern Ocean) flight campaign sampled  $N_d$  over both open water and broken ice in the seasonal sea ice zone in the Amundsen and Weddell Seas. ORCAS observed higher  $N_d$  over marginal sea ice than over open water [based on estimates of sea ice fraction (65) interpolated to the flight track; *SI Appendix*, Fig. S3C]. The high  $N_d$  over marginal sea ice observed during ORCAS (median of  $\sim 140 \text{ cm}^{-3}$ ) is consistent with the  $N_d$  observed during the OFCAP (Orographic Flow and the Climate of the Antarctic Peninsula) flights across the Antarctic peninsula (66) (*SI Appendix*, Fig. S3C) and with the

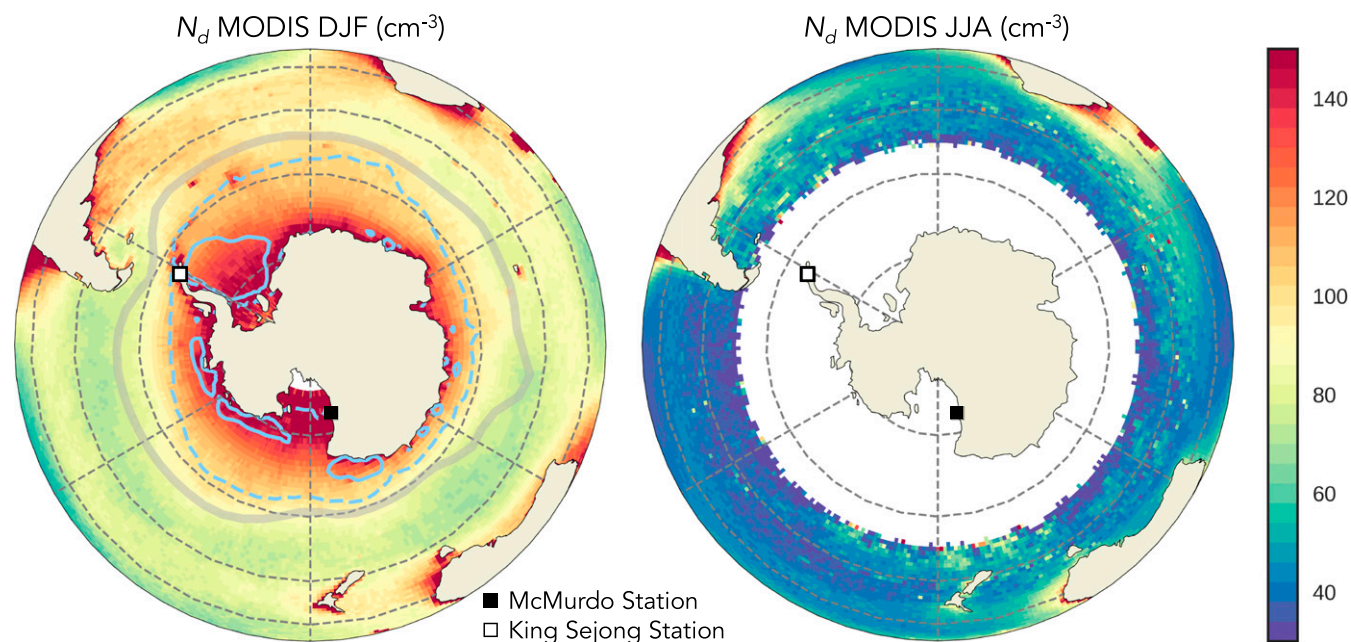


**Fig. 2.** Mean  $N_d$  calculated from MODIS data in (A) summer (DJF) and (B) winter (JJA). Seasonal mean sea ice contours from OSTIA fractional sea ice are shown as dashed (1%) and solid blue lines (50%). Locations are shown for McMurdo Station (48) (solid square) and King Sejong Station (47) (empty square). The position of the DJF lower tropospheric storm track (74) is shown with a gray line.

MODIS  $N_d$ . The increase in  $N_d$  over regions with marginal sea ice is also supported by MODIS  $N_d$  over the period 2003–2015 sampled along the ORCAS flight track (*SI Appendix, Fig. S3D*). Examination of the entire SO region by MODIS shows that, as the sea ice begins to retreat (October to November),  $N_d$  increases sharply over recently opened water (*SI Appendix, Fig. S4*), potentially linked to increases in phytoplankton productivity. Open water produces more sea spray emissions than ice-covered regions. This may also contribute to increased  $N_d$ , but with limited seasonality. In summary, in situ measurements of aerosol concentrations and aircraft measurements of  $N_d$  quantitatively support the seasonal and spatial patterns of satellite-derived  $N_d$  in the SO.

**What Does Pristine PD  $N_d$  Tell Us about GCM Discrepancies in aci?** We have demonstrated that the PD  $N_d$  hemispheric contrast is a useful framework for interpreting GCM behavior. We have also demonstrated that MODIS  $N_d$  is a reliable estimate of SH  $N_d$  as well as NH  $N_d$ . We further showed that summertime high-latitude  $N_d$  can be a factor of three smaller in GCMs than in satellite estimates (Fig. 1*A* and *B*). This leaves us with an important question: How can we use the information contained in estimates of PD  $N_d$  in pristine regions to understand what processes are currently missing or poorly captured in GCMs? Resolving these discrepancies is important for accurately representing aci occurring in the PD and PI.

In answering this question, it is important to remember that the amount of aerosol available to be activated into cloud droplets is a function of both aerosol sources and sinks. The amount of cloud droplets,  $N_d$ , will also be a function of these sources and sinks. The SO is a pristine environment where aerosol sources are analogous to the PI. However, both aerosol sources and sinks vary across the SO (see diagram in Fig. 3). Sources of SO CCN are a combination of sea spray and biogenic sources and depend upon surface and free-tropospheric physical and chemical processes (67). Emissions from ocean biology also influence NH maritime  $N_d$  and are known to control NH marine CCN and nucleation-mode seasonality (35–37). Sea spray emissions in the SH vary a small amount during the year (34, 67) and are unlikely to be contributing to the seasonal cycle of  $N_d$  (34). The dominant contributor to biogenic CCN is thought to be DMS emissions from phytoplankton with regional contributions from primary emissions of organically enriched sea spray (34, 68).

It is thought that nucleation and growth of new particles results in between 40% and 70% of global CCN (69). DMS oxidation products along with other stabilizing compounds can act as precursors for gas-to-particle conversion and form new, nucleation-mode aerosols (56, 57). New particle formation has

been documented in the free troposphere, coastal regions, at ice edges, near clouds, and in the boundary layer if conditions are favorable (57). Biogenic free tropospheric new particles are known to influence boundary layer CCN in both the NH (36) and across the SH (58, 59). SO air masses observed at the edge of Antarctica have signatures of sulfate-based new particle formation, contributing to high summertime and strongly seasonal nucleation and CCN concentrations (47, 58, 70, 71). In the Antarctic and Arctic, particle formation events are typically connected to emissions from biological activity or iodine emitted from melting ice (57, 71). In the Arctic, where seasonal ice melt increases biological activity initiating bursts of new particle formation, a ~20% summertime increase in CCN concentration can occur (72). In the Antarctic, a similar summertime increase in new particle formation over the seasonal ice zone occurs (71). Increasing concentrations of new particles during sea ice melt may be contributing to increases in  $N_d$  over retreating sea ice (*SI Appendix, Figs. S3D and S4*).

The primary sink of CCN is coalescence scavenging associated with the formation of precipitation (73). The rapid decrease in  $N_d$  off the coast of Antarctica may be related to enhanced precipitation scavenging associated with midlatitude storms (Fig. 3). This idea is supported by the location of the minima in MODIS  $N_d$  coinciding with the climatological position of the SH storm track in austral summer (Fig. 2*A*) (74). In situ measurements of trace gases and aerosol number concentration indicate that the biogenic CCN may be enhanced near Antarctica (55, 58), possibly resulting from a weakening in precipitation scavenging, an increase in biological activity near ice edge, or a combination of both effects.

To assess the role of precipitation sinks in the SO, we apply a simple source and sink budget model for CCN and, equivalently,  $N_d$  (73). The ratio between  $N_d$  and  $N_d$  computed with no precipitation loss is inversely proportional to the precipitation rate and is insensitive to the aerosol source term (see *Materials and Methods*). Unsurprisingly, the strongest precipitation sink is in the heavily precipitating SH storm track (~50°S; see  $N_d$  decrease in Fig. 1*A*), and the budget model shows that coalescence scavenging drives down  $N_d$  to ~30% of the values that would occur without a precipitation sink (exact values shown in *SI Appendix, Fig. S5 K–O*). Poleward of the storm track, at 65°S,  $N_d$  is only reduced to ~70% of the value without a precipitation sink (*SI Appendix, Fig. S5K*). This may be a reflection of marine boundary layer (MBL) depth being shallower over the cold waters near Antarctica and decreasing the clouds' capacity to support significant boundary layer cloud precipitation (75). The budget model also shows us that the fractional reduction of  $N_d$  by precipitation

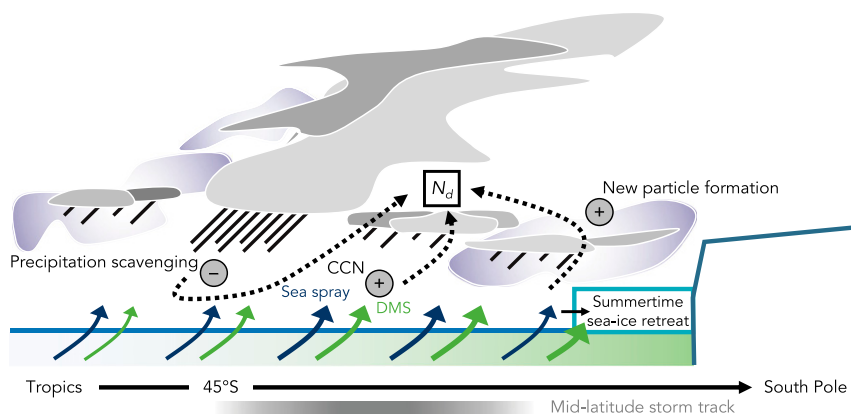


**Fig. 3.** Schematic depicting main sources (+) and sinks (–) of aerosol affecting the cloud droplet number concentration ( $N_d$ ) in the Southern Ocean. Approximate location of the climatological midlatitude storm track is shown for reference.

has only a weak seasonal cycle and is therefore not a major determinant of the seasonal  $N_d$  cycle over the SO region. This is consistent with the conclusion, from previous studies, that seasonal variability in  $N_d$  over the SO is driven primarily by biogenic aerosol sources (33, 34, 53, 76).

Based on our budget model assessment, we conclude that precipitation scavenging acts as a strong sink of CCN in the mid-latitude storm track and drives the decrease in  $N_d$  equatorward of Antarctica. There is evidence that models precipitate too much in this region, possibly creating too strong a sink of  $N_d$  in the storm track in GCMs (77). Discrepancies between satellite estimates and modeled  $N_d$  near Antarctica, where precipitation sinks of aerosol are weak, indicate that aerosol production processes are not well represented in GCMs either. It is likely that the same aerosol processes that are important near Antarctica (i.e., those linked to ocean biology) influence midlatitude regions that have stronger precipitation sinks. Missing or incomplete mechanisms for producing CCN in the biologically active region near Antarctica have implications for CCN across the SH. Disagreement between modeled and satellite estimates in summertime midlatitude  $N_d$  in the NH, which has similar marine biogenic aerosol sources, suggests that these model discrepancies are not relegated to the SH alone. GCMs may be additionally suffering from equifinality issues (43, 44). Thus, representation of the mechanisms leading to high near-Antarctic and summertime SO  $N_d$  as well as more accurate representations of precipitation sinks are important for advancing estimations of  $N_d$  in the PI and  $N_d$  in PD pristine regions.

What factors could be leading to the GCM underestimations of SO  $N_d$ ? One possibility is that GCMs do not emit enough DMS into the SO, stalling particle formation and growth processes. The amount of DMS in SO seawater and the exchange of DMS between water and air are uncertain (78). Enhancement of global DMS concentrations by 70% in HadGEM3-GA7.0 did not substantially alter SO  $N_d$  or the hemispheric contrast,  $\Delta N_{d(NH-SH)}$  (Fig. 1 and *SI Appendix, Fig. S1*). Uncertainty in air–sea exchange processes complicates this evaluation (79). However, sensitivity tests in HadGEM3-GA7.1 demonstrate that inclusion of more complete sulfate chemistry processes (relevant for summer CCN) and improved parametrizations of sea salt production (relevant for winter CCN) brings modeled  $N_d$  into closer agreement with MODIS  $N_d$  in the SO (80). Another possibility is that nucleation of new particles, particularly from DMS oxidation products, is less efficient in GCMs. If natural new particle formation mechanisms are not included in GCMs, then it is likely that models systematically overestimate the strength of aerosol–cloud radiative forcing (81). This would result in an  $RF_{aci}$  that is too strong in models, consistent with our constraint of the PPE members by  $\Delta N_{d(NH-SH)}$ .

## Discussion

The hemispheric contrast in oceanic  $N_d$  ( $\Delta N_{d(NH-SH)}$ ) offers a constraint on changes in global mean  $N_d$  between the PI and PD ( $\Delta N_{d(PD-PI)}$ ) and, by extension, on  $RF_{aci}$  (Fig. 1 *C* and *D*). Based on the satellite-derived  $\Delta N_{d(NH-SH)}$  and output from GCMs,  $\Delta N_{d(PD-PI)}$  is constrained to be between  $8 \text{ cm}^{-3}$  and  $24 \text{ cm}^{-3}$ .  $RF_{aci}$  is constrained to be between  $-1.2 \text{ W}\cdot\text{m}^{-2}$  and  $-0.6 \text{ W}\cdot\text{m}^{-2}$ . This constraint on  $RF_{aci}$  agrees with the most probable range of  $-1.2 \text{ W}\cdot\text{m}^{-2}$  to  $-0.3 \text{ W}\cdot\text{m}^{-2}$  developed in Bellouin (3). The range developed in Bellouin (3) utilized observational studies relating aerosol variance to  $N_d$  variance. Our analysis is insensitive to aerosol observations and provides an important confirmation of this range using a different approach. Our analysis also suggests that the weaker  $RF_{aci}$  in the Bellouin (3) range is not consistent with the  $N_d$  calculated from satellite data. However, an important caveat to this study and other studies seeking to offer an observational constraint on GCM behavior using a single criterion is that it may result in an overly tight constraint on model behavior due to structural uncertainties in the GCM

(42, 45). Future analysis will combine the hemispheric contrast in  $N_d$  with other constraints on model behavior to reinforce its robustness.

A key finding of this study is that models generally simulate larger hemispheric  $N_d$  differences than are calculated from satellite retrievals (Fig. 1*C*). Satellite-derived  $\Delta N_{d(NH-SH)}$  is relatively low, partly due to high local summertime  $N_d$  over the SH mid-latitudes (Fig. 1*A*). MODIS  $N_d$  near Antarctica was found to be even higher, reaching values close to those in outflows from North America and East Asia. Evaluation of in situ data from cruises, flight campaigns, and stations on the Antarctic continent confirms the accuracy of satellite-derived SO  $N_d$  (Fig. 2). Evaluation of SH CCN precipitation sinks demonstrates that high summertime  $N_d$  near Antarctica is, in part, due to low removal rates by precipitation scavenging on the poleward flank of the storm track (Fig. 3). None of the GCMs surveyed here or the 235 original PPE ensemble members come near to reproducing the high near-Antarctic values in summertime (Fig. 1; individual models and PPE members shown in *SI Appendix, Figs. S1 and S2*, respectively), suggesting models are missing key processes and/or emission sources important for CCN near Antarctica and potentially across the SH.

Ultimately,  $N_d$  is the variable that controls aci in liquid clouds. This quantity is the product of aerosol emissions, removal, transport, processing, and nucleation, and it serves as a key assessment of GCM skill in portraying aci. This reinforces the need to continue to create  $N_d$  datasets from new satellites and in new ways. We propose that future evaluations of GCM aci use the information contained within the contrast between pristine and polluted regions as an important test of realism in addition to evaluation of predicted  $N_d$  within anthropogenically perturbed regions.

## Materials and Methods

In this paper, we contrast  $N_d$  predicted by GCMs with satellite data and in situ observations.  $N_d$  is always presented in-cloud, not averaged across cloudy and cloud-free regions. The central remote sensing dataset used in this study is MODIS C5.1 utilizing the 3.7- $\mu\text{m}$  channel (82) during the period 2003–2015 (83). The calculation of  $N_d$  from MODIS retrievals of cloud optical depth ( $\tau$ ) and cloud droplet effective radius ( $r_e$ ) is not always reliable. The retrieval criteria presented in ref. 84 are used to select for times and places consistent with the assumptions made in the retrievals of  $\tau$  and  $r_e$  from satellite radiances as well as in the calculation of  $N_d$  resulting from these quantities. Briefly, these criteria are that solar zenith angles are below  $65^\circ$ , cloud tops are within 3.2 km of the surface, and liquid cloud fractions are greater than 80% in a  $1^\circ \times 1^\circ$  region (21, 84, 85). Data are filtered using these criteria based on individual level-2 swaths (as opposed to daily averages) that have been averaged to  $1^\circ \times 1^\circ$ .

Satellite-derived  $N_d$  values in the SO are evaluated using observations from a variety of campaigns and ground stations. In situ CCN observations from McMurdo Station (48) and King Sejong Station (47) are drawn from the reported monthly and seasonal mean values in the literature. MODIS  $N_d$  for these regions is shown averaged across a  $4^\circ$  box centered at the respective stations (*SI Appendix, Fig. S3A*). RITS total aerosol concentration was obtained from data provided to the Global Aerosol Synthesis and Science Project (GASSP) (86). ORCAS  $N_d$  data measured between the surface and 3 km are obtained from the Earth Observing Laboratory (EOL) at the National Center for Atmospheric Research (NCAR) (87). Sea ice cover was interpolated to the ORCAS flight track. The sea ice cover used in this analysis was from the Operational Sea Surface Temperature and Sea Ice Analysis (OSTIA) provided with the Modern-Era Retrospective analysis for Research and Applications, Version 2 (MERRA2) data product (65). The  $N_d$  calculated by MODIS is sorted as a function of sea ice vs. open water and compared to similarly separated observations from ORCAS. For the comparison in *SI Appendix, Fig. S3D*, MODIS  $N_d$  from 2003 to 2015 was restricted to only the days of the year and  $1^\circ$  regions where ORCAS measured  $N_d$ .

The GCM  $N_d$  examined in this study is provided by models participating in the Aerocom phase II indirect experiment (30), sensitivity experiments conducted in the development of HadGEM3-GA7.1 (31), and a PPE within HadGEM3-GA4-UKCA (23). The Aerocom phase II models considered are CAM5 (Community Atmosphere Model), CAM5-CLUBB (Cloud Layers Unified By Binomials), CAM5-MG2, CAM5-CLUBB-MG2, ECHAM6.1.0-HAM2.2, SPRINTARS



(Spectral Radiation-Transport Model for Aerosol Species), and SPRINTARSKK (SPRINTARS with Khairoutdinov and Kogan autoconversion scheme). The model variants of the UM (Unified Model) examined in Mulcahy et al. (31) shown here are GA7.0, GA7.1, GA7.0\_dms (DMS in sea water set to 170% of climatology), GA7.0\_act (changes to the activation scheme), and GA7.0\_comb (GA7.1 with no cloud tunings). Following standard experiment protocols for determining the anthropogenic aerosol ERF (88, 89), the model simulations and subsequent change in  $N_d$  do not account for climate-driven changes in natural aerosol emissions (e.g., wind speed changes) over the PI to PD period that may influence the  $N_d$  concentration in the SO (90).

Multimodel ensembles (such as Aerocom) are invaluable for quantifying the magnitude of differences between models due to choices of physical process representations. However, this type of ensemble neglects the uncertainty within individual models. PPEs provide a useful means of quantifying single-model uncertainty (91); however, they neglect uncertainty caused by particular choices of process representations. We represent single-model uncertainty using output from a PPE of the HadGEM-GA4-UKCA GCM. In this PPE, 26 aerosol process, emission, and deposition parameters were simultaneously perturbed, allowing for assessment of a broad range of model behavior (SI Appendix, Fig. S2). The PPE contains 235 model variants, each with a unique combination of the parameter values. Each PPE member simulated PD  $N_d$  resolved in space and time, PI global mean  $N_d$ , and top-of-the-atmosphere radiative fluxes (used to calculate  $RF_{aci}$ ). Horizontal winds and temperature fields were relaxed (92) toward 2008 meteorology from the European Centre for Medium-Range Weather Forecasts (ECMWF) Re-Analysis (ERA) ERA-Interim and forced with year 2008 anthropogenic aerosol emissions from the MACCcity emission inventory (93). To quantify uncertainty in changes over the industrial period, each of the 235 simulations has a partner simulation with identical parameter values, but with anthropogenic emissions from 1850 prescribed instead of PD emissions. The model was configured so that the first indirect effect of aerosols can be quantified in the absence of aerosol–cloud adjustments. Variations in  $N_d$  over the ensemble are caused entirely by differences in aerosol size distributions due to combinations of the 26 parameter values. We use the 235-member PPE to build statistical emulators of  $N_d$  and  $RF_{aci}$ . A sample of 1 million model variants (parameter combinations) is drawn from the emulator for each variable (32). Creation of the emulator assumes trapezoidal priors developed using expert solicitation (23). This makes the sample members more centralized in the multidimensional parameter space compared to the uniform priors assumed in earlier works (42, 45, 46, 94). If these uniform priors, which assume the entire range for all parameters are equally likely, are used in our analysis instead, the range of possible  $RF_{aci}$  consistent with estimated  $\Delta N_{d(NH-SH)}$  is between  $-1.4 \text{ W}\cdot\text{m}^{-2}$  and  $-0.5 \text{ W}\cdot\text{m}^{-2}$  (SI Appendix, Fig. S6).

Hemispheric contrast in  $N_d$  ( $\Delta N_{d(NH-SH)}$ ) is calculated as the difference in the annual mean of the area-weighted  $N_d$  concentrations over oceans 30°N to 60°N and 30°S to 60°S.  $N_d$  data in months and latitudes where MODIS retrievals are unavailable are removed from the GCM data before calculating the hemispheric contrast, to avoid biases in comparing estimates from MODIS and modeled  $N_d$ . The region 30°S to 30°N is excluded because the retrieval of  $N_d$  by MODIS in convection is less robust (21). The random uncertainty in  $N_d$  calculated from MODIS is relatively small once it is averaged across a 30°-latitude band (21). The 95% confidence on the hemispheric contrast was calculated by taking the SE in the annual hemispheric contrast in the years 2003–2015 and assuming a normal distribution. Evaluation of  $N_d$  calculated from MODIS data has shown small systematic error (21). Further, by examining the difference between hemispheres, we expect any systematic bias in the MODIS retrievals will be reduced.

The best-fit line relating  $\Delta N_{d(NH-SH)}$  to  $\Delta N_{d(PD-PI)}$  and  $RF_{aci}$  was calculated using least-squares regression on the PPE sample members. The prediction band on the best-fit line was used to quantify the possible range of  $N_d$  and  $RF_{aci}$  because all PPE sample members are considered to be equally valid representations of the real world. The prediction band about the best-fit line was calculated by fitting the 95th percentile of PPE members in 30 quantiles of hemispheric contrast.

To quantitatively estimate the impact of MBL precipitation on the seasonal climatology of  $N_d$  over the SO, we use the source and sink aerosol budget model developed in ref. 73. The model was developed for use over those parts of the global oceans where CCN concentration loss rates are driven primarily by coalescence scavenging in MBL cloud systems (95). Modeled mean MBL CCN estimates from the model appropriate for describing the monthly mean climatology of  $N_d$  were shown to agree well with the observed  $N_d$  off the coast of Chile (73) and between California and Hawaii (96).

We apply the ref. 73 model to estimate the impact of MBL cloud precipitation on the summertime meridional gradient of  $N_d$  over the SO. Using

the equilibrium number concentration from the model (ref. 73, equation 2), we construct a ratio between  $N_d$  with precipitation loss and  $N_d$  computed with no precipitation loss. This is found to be inversely proportional to the precipitation rate,

$$\frac{N_d(\text{precip})}{N_d(\text{no precip})} = \left(1 + \frac{hKP_{CB}}{Dz_i}\right)^{-1} \quad [1]$$

As in ref. 73,  $h$  is the cloud thickness (derived from MODIS LWP using the adiabatic assumption),  $K$  is a constant (97),  $P_{CB}$  is cloud base precipitation rate derived from CloudSat (73),  $D$  is the surface divergence for low cloud scenes, and  $z_i$  is the planetary boundary layer depth. Because of the difficulty of isolating surface divergence for low cloud scenes over the midlatitude storm tracks, we note that  $D^*z_i$  is the subsidence rate at cloud top, which we assume to be equal to the entrainment rate, which we estimate as 4 mm/s, consistent with typical values found in low clouds in the subtropics and midlatitudes. We estimate the coalescence scavenging sink using the CloudSat-derived precipitation rate product (98). This product attempts to estimate precipitation from all cloud systems, not only those arising from MBL clouds.

Previous applications of this model examined the eastern ocean subtropical systems (73, 96) where precipitation was primarily derived from low cloud systems. In contrast, across the SO, there is considerably more precipitation emanating from deeper precipitating systems (99). This is accounted for by only considering CloudSat precipitation estimates with detectable echo tops below 3 km altitude. This attempts to ensure that only precipitation that has a significant contribution to the coalescence scavenging of MBL CCN is used as input to the CCN and  $N_d$  budget models. This choice is based on data from the Azores, which straddles the boundary between the subtropics and the midlatitudes ( $\sim 40^\circ\text{N}$ ), showing that between 15% and 30% of all precipitation reaching the surface originated from clouds with tops below 3 km (100). Similarly, between 30°S and 70°S, with weak dependence on latitude, we find that 15 to 35% of all precipitation reaching the surface originates from clouds with tops below  $\sim 3 \text{ km}$  (SI Appendix, Fig. S5 A–E).

**Data Availability.** The observational and remote sensing datasets supporting this analysis are available either in previously published works or at supporting websites. This includes the central dataset in our analysis, the multiyear MODIS  $N_d$  product which is hosted at the Centre for Environmental Data Analysis (83). All relevant citations and supporting sites are noted in the descriptions of these datasets in *Materials and Methods*. Aerocom model simulations are similarly available from their support website (<https://aerocom.met.no>). Raw simulation output data from the HadGEM-UKCA PPE ensembles are available from the JASMIN (Joint Analysis System Meeting Infrastructure Needs) data infrastructure ([www.jasmin.ac.uk](http://www.jasmin.ac.uk)). Some of the climate-relevant fields are derived and stored for all ensemble members and made available as a community research tool.

**ACKNOWLEDGMENTS.** We thank Toshihiko Takemura for help in interpreting data from the SPRINTARS model. ORCAS Campaign data provided by NCAR/EOL under the sponsorship of NSF (<https://data.eol.ucar.edu/>). We also acknowledge support through the National Aeronautics and Space Administration (NASA) (Grant 80NSSC19K1274) for the development of the MODIS  $N_d$  product. I.L.M. and R.W. acknowledge support from NSF as part of the Southern Ocean Clouds, Radiation, Aerosol Transport Experimental Study (SOCRATES) project (Grant AGS-1660609). D.T.M. and P.R.F. acknowledge support from the Process-Based Climate Simulation: Advances in High-Resolution Modelling and European Climate Risk Assessment (PRIMAVERA) project funded by the European Union's Horizon 2020 program under Grant Agreement 641727. F.A.-M.B. was partly funded by Vetenskapsrådet Grant 2018-04274. L.R. and K.S.C. acknowledge funding from the Natural Environment Research Council (NERC) under Aerosol Model Robustness and Sensitivity Study for Improved Climate and Air Quality Prediction (AEROS), Aerosol-Cloud Interactions - A Directed Programme to Reduce Uncertainty in Forcing (ACID-PRUF), GASSP, and Aerosol-Cloud Uncertainty Reduction (A-CURE) projects (Grants NE/G006172/1, NE/I020059/1, NE/I024252/1, and NE/P013406/1) and the European Union Aerosols, Clouds, and Trace Gases Research Infrastructure (ACTRIS-2) project under Grant 262254. This work and its contributors (L.R. and K.S.C.) were supported by the UK-China Research & Innovation Partnership Fund through the Met Office Climate Science for Service Partnership China as part of the Newton Fund. D.W.-P. acknowledges funding from NERC under A-CURE and Cloud-Aerosol-Radiation Interactions and Forcing for Year 2017 (CLARIFY) (Grants NE/P013406/1 and NE/L013746/1). D.W.-P. also gratefully acknowledges the support of Amazon Web Services (AWS) through an AWS Machine Learning Research Award. D.P.G. and K.S.C. were supported by the NERC-funded North Atlantic Climate System Integrated Study (ACSIS) program via the

National Centre for Atmospheric Science (NCAS). J.P.M. was supported by the Met Office Hadley Centre Climate Programme funded by the Department for Business, Energy and Industrial Strategy (BEIS) and the Department for

Environment, Food, and Rural Affairs (DEFRA) (Grant GA01101). K.S.C. is currently a Royal Society Wolfson Merit Award holder. H.G. acknowledges support by NERC CLARIFY (Grant NE/L013479/1).

1. M. O. Andreae, C. D. Jones, P. M. Cox, Strong present-day aerosol cooling implies a hot future. *Nature* **435**, 1187–1190 (2005).
2. P. M. Forster, Inference of climate sensitivity from analysis of Earth's energy budget. *Annu. Rev. Earth Planet. Sci.* **44**, 85–106 (2016).
3. N. Bellouin *et al.*, Bounding global aerosol radiative forcing of climate change. *Rev. Geophys.* **58**, e2019RG000660 (2020).
4. S. Twomey, The influence of pollution on the shortwave albedo of clouds. *J. Atmos. Sci.* **34**, 1149–1152 (1977).
5. B. A. Albrecht, Aerosols, cloud microphysics, and fractional cloudiness. *Science* **245**, 1227–1230 (1989).
6. O. Boucher *et al.*, "Clouds and aerosols" in *Climate Change 2013: The Physical Science Basis. Contribution of Working Group I to the Fifth Assessment Report of the Intergovernmental Panel on Climate Change*, T. F. Stocker *et al.*, Eds. (Cambridge University Press, Cambridge, United Kingdom, 2013), pp. 571–657.
7. F. F. Malavelle *et al.*, Strong constraints on aerosol-cloud interactions from volcanic eruptions. *Nature* **546**, 485–491 (2017).
8. V. Toll, M. Christensen, S. Gassó, N. Bellouin, Volcano and ship tracks indicate excessive aerosol-induced cloud water increases in a climate model. *Geophys. Res. Lett.* **44**, 12,492–12,500 (2017).
9. Y. Sato *et al.*, Aerosol effects on cloud water amounts were successfully simulated by a global cloud-system resolving model. *Nat. Commun.* **9**, 985 (2018).
10. F.-M. Bender, L. Frey, D. T. McCoy, D. P. Grosvenor, J. K. Mohrmann, Assessment of aerosol–cloud–radiation correlations in satellite observations, climate models and reanalysis. *Clim. Dyn.* **52**, 4371–4392 (2019).
11. V. Toll, M. Christensen, J. Quaas, N. Bellouin, Weak average liquid-cloud-water response to anthropogenic aerosols. *Nature* **572**, 51–55 (2019).
12. E. Gryspeerdt *et al.*, Constraining the aerosol influence on cloud liquid water path. *Atmos. Chem. Phys.* **19**, 5331–5347 (2019).
13. E. Gryspeerdt, J. Quaas, N. Bellouin, Constraining the aerosol influence on cloud fraction. *J. Geophys. Res. Atmos.* **121**, 3566–3583 (2016).
14. K. S. Carslaw *et al.*, Large contribution of natural aerosols to uncertainty in indirect forcing. *Nature* **503**, 67–71 (2013).
15. L. A. Regayre *et al.*, Uncertainty in the magnitude of aerosol-cloud radiative forcing over recent decades. *Geophys. Res. Lett.* **41**, 9040–9049 (2014).
16. D. S. Hamilton *et al.*, Occurrence of pristine aerosol environments on a polluted planet. *Proc. Natl. Acad. Sci. U.S.A.* **111**, 18466–18471 (2014).
17. Q. Han, W. B. Rossow, A. A. Lacis, Near-global survey of effective droplet radii in liquid water clouds using ISCCP data. *J. Clim.* **7**, 465–497 (1994).
18. Y. Feng, V. Ramanathan, Investigation of aerosol–cloud interactions using a chemical transport model constrained by satellite observations. *Tellus B Chem. Phys. Meteorol.* **62**, 69–86 (2010).
19. O. Boucher, U. Lohmann, The sulfate-CCN-cloud albedo effect. *Tellus B Chem. Phys. Meteorol.* **47**, 281–300 (1995).
20. C. Seethala, A. Horvath, Global assessment of AMSR-E and MODIS cloud liquid water path retrievals in warm oceanic clouds. *J. Geophys. Res. D Atmos.* **115**, D13202 (2010).
21. D. P. Grosvenor *et al.*, Remote sensing of droplet number concentration in warm clouds: A review of the current state of knowledge and perspectives. *Rev. Geophys.* **56**, 409–453 (2018).
22. R. Wood, Stratocumulus clouds. *Mon. Weather Rev.* **140**, 2373–2423 (2012).
23. M. Yoshioka *et al.*, Ensembles of global climate model variants designed for the quantification and constraint of uncertainty in aerosols and their radiative forcing. *J. Adv. Model. Earth Syst.* **11**, 3728–3754 (2019).
24. D. Painemal, P. Minnis, J. K. Ayers, L. O'Neill, GOES-10 microphysical retrievals in marine warm clouds: Multi-instrument validation and daytime cycle over the southeast Pacific. *J. Geophys. Res. Atmos.* **117**, D19212 (2012).
25. M. K. Witte *et al.*, MODIS retrievals of cloud effective radius in marine stratocumulus exhibit no significant bias. *Geophys. Res. Lett.* **45**, 10,656–10,664 (2018).
26. D. Painemal, P. Zuidema, Assessment of MODIS cloud effective radius and optical thickness retrievals over the Southeast Pacific with VOCALS-REX in situ measurements. *J. Geophys. Res. D Atmos.* **116**, D24206 (2011).
27. R. Bennartz, J. Rausch, Global and regional estimates of warm cloud droplet number concentration based on 13 years of AQUA-MODIS observations. *Atmos. Chem. Phys.* **17**, 9815–9836 (2017).
28. D. T. McCoy *et al.*, Predicting decadal trends in cloud droplet number concentration using reanalysis and satellite data. *Atmos. Chem. Phys.* **18**, 2035–2047 (2018).
29. E. Ahn, Y. Huang, S. T. Siems, M. J. Manton, A comparison of cloud microphysical properties derived from MODIS and CALIPSO with in situ measurements over the wintertime Southern Ocean. *J. Geophys. Res. Atmos.* **123**, 11,120–11,140 (2018).
30. S. Ghan *et al.*, Challenges in constraining anthropogenic aerosol effects on cloud radiative forcing using present-day spatiotemporal variability. *Proc. Nat. Acad. Sci. U.S.A.* **113**, 5804–5811 (2016).
31. J. P. Mulcahy *et al.*, Improved aerosol processes and effective radiative forcing in HadGEM3 and UKESM1. *J. Adv. Model. Earth Syst.* **10**, 2786–2805 (2018).
32. D. Watson-Parris *et al.*, Constraining uncertainty in aerosol direct forcing. *Geophys. Res. Lett.* **47**, e2020GL087141 (2020).
33. G. P. Ayers, J. L. Gras, Seasonal relationship between cloud condensation nuclei and aerosol methanesulphonate in marine air. *Nature* **353**, 834–835 (1991).
34. D. T. McCoy *et al.*, Natural aerosols explain seasonal and spatial patterns of Southern Ocean cloud albedo. *Sci. Adv.* **1**, e1500157 (2015).
35. G. Zheng *et al.*, Marine boundary layer aerosol in the eastern North Atlantic: Seasonal variations and key controlling processes. *Atmos. Chem. Phys.* **18**, 17615–17635 (2018).
36. K. J. Sanchez *et al.*, Substantial seasonal contribution of observed biogenic sulfate particles to cloud condensation nuclei. *Sci. Rep.* **8**, 3235 (2018).
37. C. D. O'Dowd *et al.*, Biogenically driven organic contribution to marine aerosol. *Nature* **431**, 676–680 (2004).
38. M. Schulz *et al.*, Radiative forcing by aerosols as derived from the AeroCom present-day and pre-industrial simulations. *Atmos. Chem. Phys.* **6**, 5225–5246 (2006).
39. D. S. Hamilton *et al.*, Reassessment of pre-industrial fire emissions strongly affects anthropogenic aerosol forcing. *Nat. Commun.* **9**, 3182 (2018).
40. K. S. Carslaw *et al.*, Aerosols in the pre-industrial atmosphere. *Curr. Clim. Change Rep.* **3**, 1–15 (2017).
41. P. Stier, J. Feichter, S. Kloster, E. Vignati, J. Wilson, Emission-induced nonlinearities in the global aerosol system: Results from the ECHAM5–HAM aerosol-climate model. *J. Clim.* **19**, 3845–3862 (2006).
42. L. A. Regayre *et al.*, Aerosol and physical atmosphere model parameters are both important sources of uncertainty in aerosol ERF. *Atmos. Chem. Phys.* **18**, 9975–10006 (2018).
43. K. S. Carslaw, L. A. Lee, L. A. Regayre, J. S. Johnson, Climate models are uncertain, but we can do something about it. *Eos* **99**, 10.1029/2018EO093757 (2018).
44. L. A. Lee, C. L. Reddington, K. S. Carslaw, On the relationship between aerosol model uncertainty and radiative forcing uncertainty. *Proc. Natl. Acad. Sci. U.S.A.* **113**, 5820–5827 (2016).
45. J. S. Johnson *et al.*, The importance of comprehensive parameter sampling and multiple observations for robust constraint of aerosol radiative forcing. *Atmos. Chem. Phys.* **18**, 13031–13053 (2018).
46. L. A. Regayre *et al.*, The value of remote marine aerosol measurements for constraining radiative forcing uncertainty. *Atmos. Chem. Phys. Discuss.* **2019**, 1–11 (2019).
47. J. Kim *et al.*, Seasonal variations in physical characteristics of aerosol particles at the King Sejong Station, Antarctic Peninsula. *Atmos. Chem. Phys.* **17**, 12985–12999 (2017).
48. J. Liu *et al.*, High summertime aerosol organic functional group concentrations from marine and seabird sources at Ross Island, Antarctica, during AWARE. *Atmos. Chem. Phys.* **18**, 8571–8587 (2018).
49. E. Jang *et al.*, New particle formation events observed at the King Sejong Station, Antarctic Peninsula–Part 2: Link with the oceanic biological activities. *Atmos. Chem. Phys.* **19**, 7595–7608 (2019).
50. J. Kim *et al.*, New particle formation events observed at King Sejong Station, Antarctic Peninsula–Part 1: Physical characteristics and contribution to cloud condensation nuclei. *Atmos. Chem. Phys.* **19**, 7583–7594 (2019).
51. J. W. Fitzgerald, Marine aerosols: A review. *Atmos. Environ. A Gen. Topics* **25**, 533–545 (1991).
52. S. N. Pandis, L. M. Russell, J. H. Seinfeld, The relationship between DMS flux and CCN concentration in remote marine regions. *J. Geophys. Res.* **99**, 16945–16957 (1994).
53. G. P. Ayers, J. M. Caine, R. W. Gillett, J. P. Ivey, Atmospheric sulphur and cloud condensation nuclei in marine air in the Southern Hemisphere. *Philos. Trans. R. Soc. Lond. B Biol. Sci.* **352**, 203–211 (1997).
54. G. P. Ayers, R. W. Gillett, DMS and its oxidation products in the remote marine atmosphere: Implications for climate and atmospheric chemistry. *J. Sea Res.* **43**, 275–286 (2000).
55. J. Schmale *et al.*, Overview of the Antarctic Circumnavigation Expedition: Study of Preindustrial-like Aerosols and Their Climate Effects (ACE-SPACE). *Bull. Am. Meteorol. Soc.* **100**, 2260–2283 (2019).
56. D. Katoshevski, A. Nenes, J. H. Seinfeld, A study of processes that govern the maintenance of aerosols in the marine boundary layer. *J. Aerosol Sci.* **30**, 503–532 (1999).
57. V.-M. Kerminen *et al.*, Atmospheric new particle formation and growth: Review of field observations. *Environ. Res. Lett.* **13**, 103003 (2018).
58. R. S. Humphries *et al.*, Unexpectedly high ultrafine aerosol concentrations above East Antarctic sea ice. *Atmos. Chem. Phys.* **16**, 2185–2206 (2016).
59. D. S. Covert, V. N. Kapustin, T. S. Bates, P. K. Quinn, Physical properties of marine boundary layer aerosol particles of the mid-Pacific in relation to sources and meteorological transport. *J. Geophys. Res. D Atmos.* **101**, 6919–6930 (1996).
60. P. K. Quinn, V. N. Kapustin, T. S. Bates, D. S. Covert, Chemical and optical properties of marine boundary layer aerosol particles of the mid-Pacific in relation to sources and meteorological transport. *J. Geophys. Res. D Atmos.* **101**, 6931–6951 (1996).
61. C. W. Sullivan, C. R. McClain, J. C. Comiso, W. O. Smith, Phytoplankton standing crops within an Antarctic ice edge assessed by satellite remote sensing. *J. Geophys. Res.* **93**, 12487 (1988).
62. W. O. Smith, D. M. Nelson, Importance of ice edge phytoplankton production in the Southern Ocean. *Bioscience* **36**, 251–257 (1986).
63. K. Petrou *et al.*, Southern Ocean phytoplankton physiology in a changing climate. *J. Plant Physiol.* **203**, 135–150 (2016).
64. T. Lachlan-Cope *et al.*, On the annual variability of Antarctic aerosol size distributions at Halley research station. *Atmos. Chem. Phys. Discuss.* **20**, 4461–4476 (2020).
65. C. J. Donlon *et al.*, The operational sea surface temperature and sea ice analysis (OSTIA) system. *Remote Sens. Environ.* **116**, 140–158 (2012).



66. T. Lachlan-Cope, C. Listowski, S. O'Shea, The microphysics of clouds over the Antarctic Peninsula—Part 1: Observations. *Atmos. Chem. Phys.* **16**, 15605–15617 (2016).
67. H. Korhonen, K. S. Carslaw, D. V. Spracklen, G. W. Mann, M. T. Woodhouse, Influence of oceanic dimethyl sulfide emissions on cloud condensation nuclei concentrations and seasonality over the remote Southern Hemisphere oceans: A global model study. *J. Geophys. Res. Atmos.* **113**, D15204 (2008).
68. S. M. Burrows *et al.*, A physically based framework for modeling the organic fractionation of sea spray aerosol from bubble film Langmuir equilibria. *Atmos. Chem. Phys.* **14**, 13601–13629 (2014).
69. E. M. Dunne *et al.*, Global atmospheric particle formation from CERN CLOUD measurements. *Science* **354**, 1119–1124 (2016).
70. P. Herenz *et al.*, CCN measurements at the Princess Elisabeth Antarctica research station during three austral summers. *Atmos. Chem. Phys.* **19**, 275–294 (2019).
71. T. Lachlan-Cope *et al.*, On the annual variability of Antarctic aerosol size distributions at Halley research station. *Atmos. Chem. Phys.* **20**, 4461–4476 (2020).
72. M. Dall'Osto *et al.*, Arctic sea ice melt leads to atmospheric new particle formation. *Sci. Rep.* **7**, 3318 (2017).
73. R. Wood, D. Leon, M. Lebsock, J. Snider, A. D. Clarke, Precipitation driving of droplet concentration variability in marine low clouds. *J. Geophys. Res. Atmos.* **117**, D19210 (2012).
74. B. J. Hoskins, K. I. Hodges, A new perspective on Southern Hemisphere storm tracks. *J. Clim.* **18**, 4108–4129 (2005).
75. K. M. Chan, R. Wood, The seasonal cycle of planetary boundary layer depth determined using COSMIC radio occultation data. *J. Geophys. Res. Atmos.* **118**, 12,422–12,434 (2013).
76. N. Meskhidze, A. Nenes, Phytoplankton and cloudiness in the Southern Ocean. *Science* **314**, 1419–1423 (2006).
77. G. L. Stephens *et al.*, Dreary state of precipitation in global models. *J. Geophys. Res. D Atmos.* **115**, D24211 (2010).
78. A. Lana *et al.*, An updated climatology of surface dimethylsulfide concentrations and emission fluxes in the global ocean. *Global Biogeochem. Cycles* **25**, GB1004 (2011).
79. A. Bodas-Salcedo *et al.*, Strong dependence of atmospheric feedbacks on mixed-phase microphysics and aerosol-cloud interactions in HadGEM3. *J. Adv. Model. Earth Syst.* **11**, 1735–1758 (2019).
80. L. E. Revell *et al.*, The sensitivity of Southern Ocean aerosols and cloud microphysics to sea spray and sulfate aerosol production in the HadGEM3-GA7.1 chemistry-climate model. *Atmos. Chem. Phys.* **19**, 15447–15466 (2019).
81. H. Gordon *et al.*, Reduced anthropogenic aerosol radiative forcing caused by biogenic new particle formation. *Proc. Natl. Acad. Sci. U.S.A.* **113**, 12053–12058 (2016).
82. M. D. King *et al.*, Cloud and aerosol properties, precipitable water, and profiles of temperature and water vapor from MODIS. *IEEE Trans. Geosci. Remote Sens.* **41**, 442–458 (2003).
83. D. P. Grosvenor, R. Wood, Daily MODIS (MODerate Imaging Spectroradiometer) derived cloud droplet number concentration global dataset for 2003–2015. <https://catalogue.ceda.ac.uk/uuid/cf97ccc802d348ec8a3b6f2995dfbbff>. Accessed 15 July 2018.
84. D. P. Grosvenor, R. Wood, The effect of solar zenith angle on MODIS cloud optical and microphysical retrievals within marine liquid water clouds. *Atmos. Chem. Phys.* **14**, 7291–7321 (2014).
85. D. P. Grosvenor, O. Sourdeval, R. Wood, Parameterizing cloud top effective radii from satellite retrieved values, accounting for vertical photon transport: Quantification and correction of the resulting bias in droplet concentration and liquid water path retrievals. *Atmos. Meas. Tech.* **11**, 4273–4289 (2018).
86. C. Reddington *et al.*, The Global Aerosol Synthesis and Science Project (GASSP): Measurements and modelling to reduce uncertainty. *Bull. Am. Meteorol. Soc.* **98**, 1857–1877 (2017).
87. UCAR/NCAR - Earth Observing Laboratory, Low rate (LRT - 1 sps) navigation, state parameter, and microphysics flight-level data (Version 1.0, UCAR/NCAR - Earth Observing Laboratory, 2016). <https://doi.org/10.5065/D65T3HWR>. Accessed 4 August 2018.
88. T. Andrews, Using an AGCM to diagnose historical effective radiative forcing and mechanisms of recent decadal climate change. *J. Clim.* **27**, 1193–1209 (2014).
89. G. Myhre *et al.*, Radiative forcing of the direct aerosol effect from AeroCom phase II simulations. *Atmos. Chem. Phys.* **13**, 1853–1877 (2013).
90. H. Korhonen *et al.*, Aerosol climate feedback due to decadal increases in Southern Hemisphere wind speeds. *Geophys. Res. Lett.* **37**, L02805 (2010).
91. M. Collins *et al.*, Climate model errors, feedbacks and forcings: A comparison of perturbed physics and multi-model ensembles. *Clim. Dyn.* **36**, 1737–1766 (2010).
92. P. J. Telford, P. Braesicke, O. Morgenstern, J. A. Pyle, Technical note: Description and assessment of a nudged version of the new dynamics Unified Model. *Atmos. Chem. Phys.* **8**, 1701–1712 (2008).
93. C. Granier *et al.*, Evolution of anthropogenic and biomass burning emissions of air pollutants at global and regional scales during the 1980–2010 period. *Clim. Change* **109**, 163–190 (2011).
94. J. S. Johnson *et al.*, Robust observational constraint of uncertain aerosol processes and emissions in a climate model and the effect on aerosol radiative forcing. *Atmos. Chem. Phys. Discuss.* **2019**, 1–51 (2019).
95. R. Wood, Rate of loss of cloud droplets by coalescence in warm clouds. *J. Geophys. Res. D Atmos.* **111**, D21205 (2006).
96. J. Mohrmann, R. Wood, J. McGibbon, R. Eastman, E. Luke, Drivers of seasonal variability in marine boundary layer aerosol number concentration investigated using a steady state approach. *J. Geophys. Res. D Atmos.* **123**, 1097–1112 (2018).
97. R. Wood, Relationships between optical depth, liquid water path, droplet concentration, and effective radius in an adiabatic layer cloud. [https://atmos.uw.edu/~robwood/papers/childean\\_plume/optical\\_depth\\_relations.pdf](https://atmos.uw.edu/~robwood/papers/childean_plume/optical_depth_relations.pdf). Accessed 15 July 2018.
98. J. M. Haynes *et al.*, Rainfall retrieval over the ocean with spaceborne W-band radar. *J. Geophys. Res. D Atmos.* **114**, D00A22 (2009).
99. Z. Wang, S. T. Siems, D. Belusic, M. J. Manton, Y. Huang, A climatology of the precipitation over the Southern Ocean as observed at Macquarie Island. *J. Appl. Meteorol. Climatol.* **54**, 2321–2337 (2015).
100. R. Wood *et al.*, Clouds, aerosols, and precipitation in the marine boundary layer: An arm mobile facility deployment. *Bull. Am. Meteorol. Soc.* **96**, 419–440 (2015).